

RESEARCH ARTICLE | JULY 01 2024

Multi-delay coherence imaging spectroscopy optimized for ion temperature measurements in the divertor plasma of the Wendelstein 7-X stellarator

David M. Kriete ; Valeria Perseo ; Dorothea Gradic ; David A. Ennis ; Ralf König ; David A. Maurer ; W7-X Team

 Check for updates

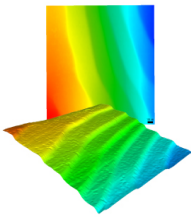
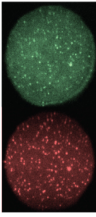
Rev. Sci. Instrum. 95, 073503 (2024)

<https://doi.org/10.1063/5.0208586>


View
Online


Export
Citation

08 July 2024 14:04:22

 <p>MCL MAD CITY LABS INC. www.madcitylabs.com</p>	<p>Nanopositioning Systems</p> 	<p>Modular Motion Control</p> 	<p>AFM and NSOM Instruments</p> 	<p>Single Molecule Microscopes</p> 
--	--	--	---	--

Multi-delay coherence imaging spectroscopy optimized for ion temperature measurements in the divertor plasma of the Wendelstein 7-X stellarator

Cite as: Rev. Sci. Instrum. 95, 073503 (2024); doi: 10.1063/5.0208586

Submitted: 15 March 2024 • Accepted: 12 June 2024 •

Published Online: 1 July 2024



View Online



Export Citation



CrossMark

David M. Kriete,^{1,a)} Valeria Perseo,² Dorothea Gradic,² David A. Ennis,¹ Ralf König,²
David A. Maurer,¹ and W7-X Team^{2,b)}

AFFILIATIONS

¹Department of Physics, Auburn University, Auburn, Alabama 36849, USA

²Max-Planck-Institut für Plasmaphysik, Greifswald, Mecklenburg-Vorpommern 17491, Germany

^{a)}Author to whom correspondence should be addressed: kriete@auburn.edu

^{b)}For the full list of the W7-X Team members, see the author list of T. S. Pedersen *et al.*, Nucl. Fusion **62**, 042022 (2022).

ABSTRACT

A new coherence imaging spectroscopy (CIS) diagnostic optimized to measure the C^{2+} impurity ion temperature T_i spatial distribution in the divertor plasma of the W7-X stellarator is designed, tested, and validated. Using CIS to obtain T_i in the edge of magnetically confined plasmas has historically been challenging because Doppler broadening and Zeeman splitting have comparable effects on the shape of spectral emission lines. To distinguish between these two mechanisms, a novel approach to birefringent crystal design is employed to minimize the diagnostic's sensitivity to Zeeman splitting. The recently developed pixelated multi-delay CIS approach is also used to obtain four times as much spectral information as traditional CIS approaches. The T_i -optimized CIS diagnostic is validated in a long-pulse W7-X plasma by comparison with a high-resolution spectrometer whose sightlines overlap with the CIS field of view. The CIS and spectrometer T_i profiles have the same shape and agree to within 10% on average and 25% in the worst case. Images of the T_i distribution near the divertor show toroidally elongated bands aligned with the magnetic field, with T_i ranging between 10 and 40 eV.

© 2024 Author(s). All article content, except where otherwise noted, is licensed under a Creative Commons Attribution (CC BY) license (<http://creativecommons.org/licenses/by/4.0/>). <https://doi.org/10.1063/5.0208586>

I. INTRODUCTION

The temperature of main and impurity ions plays a crucial role in the scrape-off layer (SOL) plasma that forms the interface between the confined plasma core and the first wall in magnetic confinement fusion experiments. The ion temperature T_i controls the impact energy of ions on plasma-facing components (PFCs), which strongly affects material erosion rates that will ultimately limit the lifetime of PFCs in a fusion reactor and source impurities that can be transported into the core, causing degradation of plasma performance.¹ Knowledge of the T_i distribution in the SOL is also useful for understanding the exhaust of heat and particles from the core plasma to the divertor, as T_i influences the ion sound speed and

sheath heat transmission coefficients that form the boundary conditions at the divertor. While T_i has been characterized in many tokamak SOLs,² there is only scarce T_i information in the SOL of stellarators. To address this need, we advance the coherence imaging spectroscopy technique to image the ion temperature distribution across the island divertor of the Wendelstein 7-X (W7-X) stellarator.

In the SOL plasma, measuring T_i is more difficult than other parameters, such as electron temperature and density, which are readily attainable from Langmuir probes.³ The main diagnostic used for SOL T_i measurements is the retarding field analyzer³ (RFA), and a radially scanning RFA has previously been used to obtain T_i profiles in a W7-X SOL island located in a gap between the toroidally discontinuous divertors.^{4,5} To obtain T_i information near

the W7-X divertor, a high-wavelength-resolution dispersive spectrometer has been employed to infer the temperatures of impurity ions,⁶ which may be representative of the main ion temperature if the charge state of the emitting impurity ion species is high enough. Due to the fully 3D nature of stellarator SOLs, parameters have to be measured at many spatial locations to fully characterize the SOL plasma distribution and validate the edge simulation tools needed to design divertors in future devices. This motivates the use of coherence imaging spectroscopy (CIS) to obtain the T_i distribution with a much higher degree of spatial information than is feasible with dispersive spectrometers. Impurity T_i images have previously been obtained using a CIS diagnostic designed for flow velocity measurements⁷ by calibrating it with a high-resolution spectrometer.⁸ However, this cross-calibration approach is only valid in a small region of the image with overlapping spectrometer sightlines, limiting the available spatial information.

In this paper, we design, test, and validate a coherence imaging spectroscopy instrument optimized specifically for T_i measurements. This builds on the prior work of Ref. 8 by developing a CIS diagnostic that can obtain high-resolution T_i images without requiring cross-calibration with a high-resolution spectrometer. Section II gives an overview of the CIS technique and describes the basic principles behind measuring T_i with CIS. Section III explains how to optimize a CIS diagnostic for T_i . Section IV presents the design of the W7-X T_i -optimized CIS diagnostic and characterizes its parameters. Section V describes the analysis procedure used to infer T_i from the CIS raw data. Section VI compares CIS measurements in a W7-X plasma against those from a high-resolution spectrometer, validating the ability of CIS to image the T_i distribution near the divertor. Section VII summarizes and discusses the results of this work and presents avenues for future work.

II. PRINCIPLES OF T_i MEASUREMENTS WITH COHERENCE IMAGING SPECTROSCOPY

A. Coherence imaging spectroscopy overview

Coherence imaging spectroscopy is a plasma diagnostic technique that provides high-spatial-resolution images of ion and neutral spectroscopic information, including flow velocities and temperatures.⁹ The most common variant of CIS in use today is the spatial heterodyne approach.^{9,10} This approach employs a polarization interferometer to encode information about line-integrated Doppler parameters into a linear fringe pattern that is overlaid on an image of spectral line emission. Shifts of the fringes, i.e., phase shifts, are related to shifts in the wavelength of the spectral line, allowing flow velocity to be obtained via the Doppler shift. The contrast of the fringe pattern is related to the width of the spectral line, allowing temperature to be obtained by relating the contrast to the Doppler-broadened spectral width.

We now briefly describe how CIS works, referring the reader to Refs. 9 and 11 for a more comprehensive explanation. A spatial heterodyne polarization interferometer uses a combination of optical filters, polarizers, and birefringent crystals to create a spatial interference pattern. Incoming light first passes through a narrowband filter to isolate a spectral line from a single ion or neutral species. The polarizers and birefringent crystals then effectively split the light into two orthogonally polarized beams and introduce a phase delay

between them. When the beams recombine at the camera sensor, this produces a signal,

$$S = \frac{I}{4} (1 + \zeta \cos(\Phi)), \quad (1)$$

where I is the input light intensity into the first polarizer, Φ is the phase delay between the two beams, and ζ is the contrast, which depends on the spectral width of the light.

The phase delay depends on the angle that a light ray takes through the crystals and is scanned linearly across the image,¹² producing nearly straight fringes. The phase delay also depends on wavelength, causing the fringes to shift when the wavelength of the emission line changes. The variation of Φ with respect to wavelength λ , called the group delay, is a key parameter characterizing the spectral response of a CIS instrument. Throughout this paper, we use the normalized group delay, which is defined as

$$\hat{N}(\lambda) = -\frac{\lambda}{2\pi} \frac{d\Phi}{d\lambda}. \quad (2)$$

When a narrowband spectrum with centroid wavelength λ_0 passes through the CIS interferometer, the fringe pattern encodes the complex coherence of the light, $\Gamma = I\zeta \exp(i\Phi)$, at the interferometer's group delay. The coherence is related to the spectral intensity $I(\lambda)$ by a Fourier transform,

$$\Gamma(\hat{N}) = \int I(\lambda) \exp[-2\pi i \hat{N}(\lambda - \lambda_0)/\lambda_0] d\lambda. \quad (3)$$

Therefore, CIS is a type of Fourier transform spectrometer.

The main challenge measuring ion temperatures with CIS is isolating the Doppler-broadening contribution to the overall linewidth from the contributions of other line-broadening mechanisms. In addition to Doppler broadening, which depends on ion temperature, the linewidth is affected by Zeeman splitting, which depends on magnetic field, and Stark broadening, which depends mainly on electron density. CIS also cannot easily distinguish between line emission and background continuum emission, e.g., bremsstrahlung or thermal emission from hot plasma-facing components. In the hot plasma core, Doppler broadening typically dominates the other line-broadening mechanisms, making the inference of T_i comparatively simple. This has been used to image the core T_i profile with CIS via charge-exchange recombination spectroscopy.¹³⁻¹⁵ In the SOL, the various line-broadening mechanisms can be comparable in strength, making it difficult to isolate the Doppler broadening contribution because CIS obtains a limited amount of spectral information. Ion temperature measurements with CIS then require a combination of assumptions or prior information to constrain the various line-broadening mechanisms, using a multi-delay CIS configuration to increase the available spectral information, and/or optimizing the CIS instrument to be more sensitive to Doppler broadening than the other line-broadening mechanisms.

B. Relationship between phase/contrast and ion parameters

To extract ion parameters from a CIS image, the interference pattern is first demodulated to obtain the intensity I , phase Φ , and

contrast ζ for every pixel. The measured phase and contrast are given by

$$\Phi_{\text{meas}} = \Phi_{\text{D}} + \Phi_{\text{MZ}} + \Phi_0, \quad (4)$$

$$\zeta_{\text{meas}} = \zeta_{\text{D}} \zeta_{\text{MZ}} \zeta_{\text{S}} \zeta_{\text{B}} \zeta_{\text{I}}, \quad (5)$$

where $\Phi_{\text{D}}/\zeta_{\text{D}}$ is the phase/contrast induced by the Doppler effect; $\Phi_{\text{MZ}}/\zeta_{\text{MZ}}$ is the multiplet-Zeeman phase/contrast, which arises from spectral line splitting due to fine structure and the Zeeman effect; ζ_{S} is the contrast from Stark broadening; ζ_{B} is the contrast reduction due to background emission; Φ_0 is the phase at the centroid wavelength of the spectral line; and ζ_{I} is the instrument contrast.¹¹ We now discuss each of these terms in detail.

1. Doppler phase/contrast

The Doppler phase is directly proportional to the velocity of the ion species \mathbf{v}_i ,

$$\Phi_{\text{D}} = -2\pi \hat{N}_0 \mathbf{v}_i \cdot \hat{\ell} / c, \quad (6)$$

where $\hat{N}_0 = \hat{N}(\lambda_0)$ is the group delay at the centroid wavelength λ_0 of the spectral line, $\hat{\ell}$ is the unit vector directed along the sightline for each pixel in the image, and c is the speed of light. The Doppler contrast is related to the ion temperature by

$$\zeta_{\text{D}} = e^{-T_i/T_C}, \quad (7)$$

$$T_C = \frac{m_i c^2}{2\pi^2 \hat{N}_0^2}. \quad (8)$$

Here, m_i is the ion mass and T_C is the instrument's characteristic temperature, which is a metric for sensitivity to T_i .

2. Multiplet-Zeeman phase/contrast

Splitting of a spectral line due to both fine structure and the Zeeman effect alters the phase and contrast. Lines with fine structure, also called multiplet lines, have several components that undergo different amounts of Zeeman splitting. These two effects are treated together by first calculating the multiplet-Zeeman coherence,¹¹

$$\gamma_{\text{MZ}} = \sum_c A_c \exp[2\pi i \hat{N}_0 (\lambda_0 - \lambda_c) / \lambda_c], \quad (9)$$

where the sum is carried out over all multiplet-Zeeman components, each labeled 'c'; A_c is the normalized amplitude of component c; and λ_c is the wavelength of component c. The multiplet-Zeeman phase and contrast are then given by $\Phi_{\text{MZ}} = \arg(\gamma_{\text{MZ}})$ and $\zeta_{\text{MZ}} = |\gamma_{\text{MZ}}|$.

Zeeman splitting depends on the magnetic field strength B and the angle α between the magnetic field and diagnostic sightline. The multiplet-Zeeman components for a given B and α are calculated using a code developed in Refs. 8, 16, and 17 and accessible in the ADAS603 database.¹⁸ The Zeeman π and σ components have different polarization, so they can be attenuated differently by the first polarizer of the CIS optics. Generally, this must be taken into account during CIS design and analysis. However, the W7-X CIS diagnostic uses an imaging fiber bundle to couple light from

the plasma into the CIS optics, which scrambles polarization information. Therefore, throughout the rest of this work, the Zeeman component amplitudes returned directly by the Zeeman code are used.

Note that multiplet components must be accounted for when calculating the centroid wavelength of a spectral line,

$$\lambda_0 = \frac{1}{\sum_c A_c / \lambda_c}. \quad (10)$$

However, Zeeman splitting has no effect on λ_0 because each multiplet component is split symmetrically. For singlet lines, Zeeman splitting similarly has no effect on the phase, but for multiplet lines, Zeeman splitting is not symmetric about λ_0 , so it does alter the phase.

3. Stark contrast

Stark broadening mainly depends on the electron density n_e but also has weak dependencies on T_e and T_i .^{19,20} There is no general formula for Stark broadening, but a database of precomputed line shapes is available for diagnostic use.²⁰ For $n_e > 10^{20} \text{ m}^{-3}$ and $T_i \sim 1 \text{ eV}$, the Stark contrast is approximately given by²¹

$$\zeta_{\text{S}} \approx \exp[-(n_e/n_C)^{2/3}], \quad (11)$$

$$n_C = \left(\frac{\lambda_0}{A\pi |\hat{N}_0|} \right)^{3/2}, \quad (12)$$

where n_C is the instrument's characteristic density and A is a coefficient that depends on the spectral line. In the edge plasmas of W7-X, Stark broadening has only been observed for hydrogen Balmer lines and is negligible for impurity lines.⁶

4. Background contrast

The effect of background emission on phase and contrast is, in general, more complicated than shown in Eqs. (4) and (5). However, when the filter width $\Delta\lambda$ is large enough, such that $\hat{N}\Delta\lambda/\lambda_0 \gg 1$ wave, background emission does not affect the phase and affects the contrast only by a multiplicative factor ζ_{B} . This condition is typically satisfied in the visible spectrum for the $\Delta\lambda \gtrsim 1 \text{ nm}$ filters used by CIS. The background contrast is related to the signal-to-background ratio (SBR) by

$$\zeta_{\text{B}} = \frac{\text{SBR}}{1 + \text{SBR}} = \frac{\int I_L(\lambda) d\lambda}{\int I_B(\lambda) d\lambda + \int I_L(\lambda) d\lambda}, \quad (13)$$

where I_L and I_B are the spectral intensities from line and background emission, respectively, and the integrals are performed over the width of the filter.

5. Instrument phase/contrast

The centroid phase and instrument contrast are the values that arise for an input source of monochromatic light at λ_0 . The centroid phase is highly sensitive to ambient temperature, so on W7-X, Φ_0 is measured immediately before and after every plasma discharge by using a remote-controlled mirror to introduce light from a calibration system into the CIS optics.⁷ The calibration system consists of an integrating sphere illuminated by a precision tunable continuous-wave laser (C-WAVE VIS from HÜBNER Photonics), which can

calibrate many spectral lines of interest in the visible range at their unshifted centroid wavelength.^{7,22} This eliminates errors associated with extrapolating Φ_0 from the wavelength of a nearby spectral lamp line^{23–25} or generating Φ_0 from a fitted model of an ideal birefringent crystal.²⁶ The instrument contrast is analogous to the instrument function width of a dispersive spectrometer. An ideal instrument has $\zeta_1 = 1$, but inhomogeneities in the crystals, aberrations in the imaging optics, and the finite size of the camera pixels all reduce ζ_1 .

III. CIS INSTRUMENT DESIGN FOR SOL T_i MEASUREMENTS

A. Spectral line selection

The choice of which spectral line to observe strongly affects the ability to measure T_i and involves the following considerations:

- The observed spectral line must be bright enough to have sufficient signal-to-noise ratio and signal-to-background ratio.
- Emission should occur in the desired region of the plasma, e.g., scrape-off layer or core. Ideally, the emission is localized to a small region to facilitate the inference of plasma parameters from the raw data.
- The observed spectral line should be separated from nearby contamination lines by ≥ 1 nm, which is the current lower limit on the bandwidth of commercially available optical bandpass filters.
- Fine structure in the line shape can allow continuous broadening mechanisms, i.e., Doppler/Stark broadening, to be more easily distinguished from splitting mechanisms, i.e., Zeeman splitting (see Sec. III B).

For T_i measurements in the SOL of W7-X, we use the C III ($2s3p\ ^3P \rightarrow 2s3s\ ^3S$) 465 nm line. As W7-X has carbon plasma-facing components, this spectral line is among the brightest in the visible range, yielding high signal-to-noise and signal-to-background ratios across the entire SOL parameter range for the 50 ms exposure time typically used by the CIS camera. Because of this, $\zeta_B \approx 1$ and can largely be neglected. High-resolution spectrometer measurements in W7-X show no evidence of Stark broadening for this C III line,⁶ so Stark broadening is also neglected. This leaves Doppler broadening and multiplet-Zeeman splitting as the primary mechanisms contributing to the measured phase and contrast.

Emission from the C III line generally occurs in regions where $T_e = 3\text{--}10$ eV, peaking around 6 eV, although charge-exchange reactions and transport effects can extend the upper temperature range.²⁷ In W7-X, T_e at the separatrix is usually ≈ 100 eV,²⁸ so emission is outside the separatrix; its precise location depends on the SOL T_e and carbon density distributions. However, in deeply detached plasmas, the separatrix T_e falls below 20 eV and C III emission moves inside the separatrix.^{29,30} The thermal equilibration time between carbon and main ions ranges $10^{-2}\text{--}10^0$ ms over the W7-X SOL parameter space ($n = 10^{18}\text{--}10^{20}$ m⁻³, $T = 10\text{--}100$ eV). This is shorter than the ~ 10 ms transport timescale³¹ and the lifetime of the C²⁺ charge state,³² so carbon ion temperatures derived from the C III line are representative of the main ion temperature.

B. T_i -optimized birefringent crystals

Specially designed crystals can exploit the fine structure in a spectral line to give a CIS instrument higher sensitivity to Doppler broadening, and hence T_i , than to Zeeman splitting. This is illustrated for \perp -to- B viewing of the C III line by Fig. 1. The contrast arising from Doppler broadening, as defined by Eq. (7), decreases monotonically with increasing T_i and group delay [Fig. 1(a)]. The multiplet-Zeeman contrast, as determined from Eq. (9), instead goes through a series of maxima and minima with increasing group delay [Fig. 1(b)]. Generally, ζ_{MZ} decreases with increasing B , but at the minima ($\hat{N} = 700, 2600,$ and 4100 waves), it is almost entirely independent of B . A crystal whose group delay is at one of these ζ_{MZ} minima will thus have low sensitivity to Zeeman splitting.

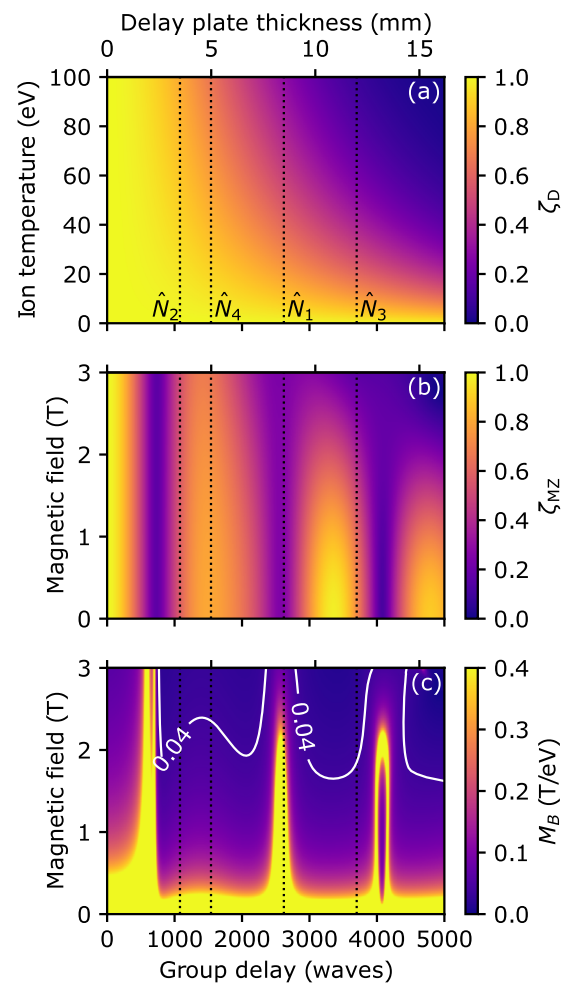


FIG. 1. Group delay dependence of (a) Doppler contrast ζ_D , (b) multiplet-Zeeman contrast ζ_{MZ} , and (c) ion-temperature-to-magnetic-field sensitivity M_B for viewing geometry perpendicular to the magnetic field. The top axis of each subplot gives a mapping from group delay to thickness of an alpha-barium-borate delay plate. The black dashed lines denote the four group delays of the W7-X CIS instrument. The region below the white $M_B = 0.04$ T eV⁻¹ contour has higher sensitivity to T_i than B for the expected W7-X scrape-off layer plasma parameters.

Quantifying the relative sensitivity to Doppler broadening vs Zeeman splitting enables a crystal to be optimized for T_i measurements. The sensitivity to T_i , i.e., the fractional change in contrast per unit change in T_i , is

$$S_{T_i} \equiv \frac{1}{\zeta_D} \frac{d\zeta_D}{dT_i} = -\frac{1}{T_C}. \quad (14)$$

Note that S_{T_i} is independent of T_i and depends only on the group delay, through T_C . The multiplet-Zeeman contrast depends on both magnetic field B and field-sightline angle α , so there are two sensitivities,

$$S_B \equiv \frac{1}{\zeta_{MZ}} \frac{d\zeta_{MZ}}{dB}, \quad (15)$$

$$S_\alpha \equiv \frac{1}{\zeta_{MZ}} \frac{d\zeta_{MZ}}{d\alpha}. \quad (16)$$

Both S_B and S_α depend on B , α , and \hat{N} , and they are calculated numerically. For the C III line, $S_B \gg S_\alpha$, so only the magnetic field sensitivity needs to be considered. The relative sensitivity of a crystal to T_i vs B is then quantified by $M_B \equiv S_{T_i}/S_B$, which is shown in Fig. 1(c).

For full-field W7-X operation, $B = 2.2\text{--}2.8$ T in the SOL. In low density plasmas with decoupled ions and electrons, $T_i = 5\text{--}100$ eV could be possible, but in higher density plasmas with $T_i \approx T_e$, a more realistic expectation is $T_i = 5\text{--}20$ eV. With these expected parameter ranges, a crystal will be more sensitive to T_i than B when $M_B \gtrsim \Delta B/\Delta T_i = (0.6 \text{ T})/(15 \text{ eV}) = 0.04 \text{ T eV}^{-1}$. Figure 1(c) shows that in the $B = 2.2\text{--}2.8$ T range, this condition is satisfied for \hat{N} near 700, 2600, and 4100 waves. These coincide with the minima in ζ_{MZ} because at these locations S_B is small. For these group delays, $\zeta_{MZ} = 0.17, 0.26$, and 0.14 , respectively. The optimal group delay is then 2600 waves because it has the highest contrast, and therefore, lowest measurement uncertainty, of the three high-relative-sensitivity values.

The optimal group delay does not change with field-sightline angle, so the above-mentioned result obtained for perpendicular viewing geometry ($\alpha = 90^\circ$) is also valid for parallel viewing geometry ($\alpha = 0^\circ$). However, as α approaches 0° , Zeeman splitting has a stronger effect on the contrast because π components, which are near the center of the line, become suppressed relative to σ components, which tend to be concentrated toward the wings of the line. This reduces M_B , making perpendicular viewing geometry better suited for T_i measurements than parallel viewing geometry.

The group delay of a crystal depends on its material, thickness, and cut angle, i.e., the angle between its optic axis and front surface. For an arbitrary crystal specification, the nominal group delay can be calculated by numerically differentiating the Veiras phase delay equation [Eq. (12) in Ref. 12]. The W7-X CIS diagnostic uses crystals made of alpha barium borate (α -BBO) due to its low sensitivity to ambient temperature drifts.⁷ Measurements of the group delay are typically within 5% of the nominal value, and the main source of error is suspected to be uncertainty in the refractive index data for α -BBO.^{26,33} The top axis of each plot shown in Fig. 1 gives the thickness of an α -BBO delay plate (0° cut angle) that produces the group delay on the bottom axis.

In addition to the group delay, crystal specification affects the fringe wavelength. Smaller fringe wavelength improves spatial res-

olution but reduces instrument contrast. The fringe wavelength in pixels is given by

$$d_{\text{fringe}} = \frac{f\lambda}{pL} \frac{n_e^2 \sin^2(\theta) + n_o^2 \cos^2(\theta)}{n(n_o^2 - n_e^2) \sin(\theta) \cos(\theta)}, \quad (17)$$

where f is the imaging lens focal length, p is the camera pixel size, L is the crystal thickness, θ is the crystal cut angle, n is the air refractive index, and n_o/n_e are the crystal ordinary/extraordinary refractive indices.¹² In the range of $\theta = 0^\circ\text{--}45^\circ$, d_{fringe} increases with decreasing θ and L . In contrast, the group delay increases with L but decreases with θ . This allows the desired group delay and fringe wavelength to be achieved by suitable choice of f , L , and θ , subject to constraints on commercially available crystals and imaging lenses.

While here we optimized the crystal for maximum T_i sensitivity relative to B sensitivity, other optimization objectives could be used. A group delay of 1500 waves would maximize ζ_{MZ} and, therefore, minimize the measurement's statistical uncertainty. A group delay of 3450 waves would maximize the sensitivity to magnetic field and could potentially be used to measure the location of C III emission if the B distribution is known throughout the plasma.

Finally, we emphasize that crystal optimization only works for spectral lines with appropriately spaced fine structure components. For singlet lines, or lines whose components are spaced so closely together that they effectively behave as a singlet, both ζ_D and ζ_{MZ} decrease monotonically with group delay and M_B is effectively constant. The spacing between fine structure components needs to be $\gtrsim 0.1$ nm for group delay optimization to be possible given the ~ 20 mm practical upper limit on crystal thickness. However, the spacing cannot be too large or the maxima/minima in ζ_{MZ} will be spaced so closely together that the required tolerance on a crystal's group delay becomes unachievable.

C. Multi-delay CIS configuration

Measuring the coherence at multiple group delays increases the obtained spectral information and helps distinguish between different line-broadening mechanisms, improving the accuracy of T_i measurements. The conceptually simplest approach of obtaining information at multiple delays is to measure repeat plasma discharges with different crystal configurations.³⁴ However, this approach is time-intensive and susceptible to discharge-to-discharge variations, so CIS configurations that measure at multiple delays simultaneously have been developed. These include splitting the light from the plasma across multiple images each with a different crystal,¹⁴ encoding the coherence into multiple linear fringe patterns within a single image,¹⁴ and using a camera with a polarized sensor to encode the coherence into linear and pixelated fringe patterns.³⁵

In this work, we use the linear and pixelated fringe multi-delay configuration,³⁵ which obtains the coherence at four group delays simultaneously. A simplified schematic and a picture of the multi-delay CIS instrument used on W7-X are shown in Fig. 2. Light from the plasma is collected with a lens and relayed to the CIS instrument via an imaging fiber bundle (not shown here; see Ref. 7 for details of the light collection optics). The components up through the second polarizer are identical to that of a single-delay CIS instrument and produce linear fringes that encode the coherence at the displacer plate's group delay: $\hat{N}_1 = \hat{N}_{\text{displacer}}$. The delay plate, quarter-wave plate (QWP), and polarized camera together produce an additional

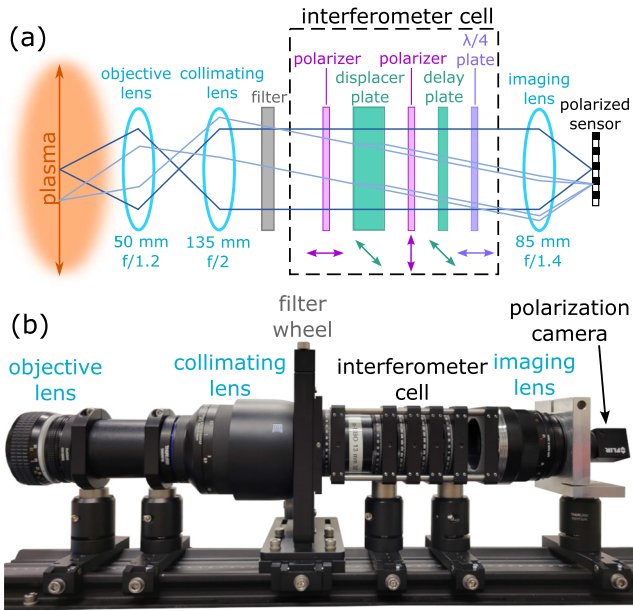


FIG. 2. (a) Schematic and (b) picture of the multi-delay CIS instrument used on W7-X. The arrow beneath each component in the interferometer cell denotes the rotational orientation of its optic axis.

pixelated fringe pattern encoding the coherence at the delay plate's group delay: $\hat{N}_2 = \hat{N}_{\text{delay}}$. The linear and pixelated fringe patterns are also multiplied together, producing two mixed fringe patterns at group delays of $\hat{N}_3 = \hat{N}_{\text{delay}} + \hat{N}_{\text{displacer}}$ and $\hat{N}_4 = \hat{N}_{\text{delay}} - \hat{N}_{\text{displacer}}$.

The multi-delay fringe pattern is given by Eq. (10) in Ref. 35,

$$S = \frac{I}{8} \left[1 + \zeta_1 \cos(\Phi_1) + \zeta_2 \cos(\Phi_2) + \frac{1}{2} \zeta_3 \cos(\Phi_3) + \frac{1}{2} \zeta_4 \cos(\Phi_4) \right], \quad (18)$$

where Φ_k/ζ_k is the phase/contrast encoded at \hat{N}_k and k is a label for the four fringe patterns. The fringe amplitude is $I\zeta(\hat{N})/8$ for the pure linear and pixelated fringe patterns (1 and 2), which each arise from a single crystal, while the amplitude is half as large for the two mixed fringe patterns (3 and 4) that arise from combinations of both crystals. Measurements at \hat{N}_1 and \hat{N}_2 , therefore, have higher signal-to-noise ratio than those at \hat{N}_3 and \hat{N}_4 , so optimized group delay values determined using the guidelines in Sec. III B should be generated by a single crystal instead of combinations of crystals. The fringe amplitude of a single-delay CIS configuration is $I\zeta(\hat{N})/4$ [see Eq. (1)], twice as high as the multi-delay linear and pixelated fringe amplitudes. This highlights one of the main trade-offs with the multi-delay approach: more spectral information at the cost of reduced light throughput.

IV. DESIGN POINT AND CHARACTERIZATION OF THE W7-X SOL T_i INSTRUMENT

For the W7-X T_i -optimized CIS instrument, an 11 mm crystal with a 30° cut angle was procured, which has a nominal group delay of $\hat{N}_1 = 2620$ waves and a fringe wavelength of 16 pixels when used with an 85 mm focal length imaging lens. A 3.5 mm delay plate with

a nominal group delay of $\hat{N}_2 = 1080$ waves was chosen from the stock of crystals already available at W7-X, yielding expected values of $\hat{N}_3 = 3700$ waves and $\hat{N}_4 = -1540$ waves (note that the sign of \hat{N} does not affect the contrast). \hat{N}_4 is near a multiplet-Zeeman contrast maximum, so it produces data with relatively high signal-to-noise ratio, while \hat{N}_2 and \hat{N}_3 are about halfway between minima and maxima [Fig. 1(b)]. An achromatic QWP with a 420–1100 nm wavelength range is used to allow observation of lines across the visible spectrum without having to realign the interferometer cell. The camera is a FLIR Blackfly S with a Sony IMX250MZR polarization sensor, which has 2448×2048 resolution, $3.45 \mu\text{m}$ pixel size, and 12 bit dynamic range.

The instrument's four group delays are measured by scanning the wavelength of the C-WAVE calibration laser.^{7,22} Figure 3 shows the variation of the phase for each fringe pattern averaged over a 100×100 pixel region at the image center during the course of a ± 15 pm laser scan centered on the C III multiplet at 465 nm. The normalized group delay is calculated from the slope of each phase vs wavelength line using Eq. (2). The displacer plate's measured group delay agrees with its nominal 2620 waves value within the measurement's approximately ± 10 waves uncertainty. The delay plate's group delay of 1130 waves is 4% larger than its nominal 1080 waves value, but this deviation is small enough that there is no adverse impact on the instrument's ability to measure T_i .

Laser scans also allow the spatial variation of the group delay across the image to be determined. Figure 4 shows the deviation of the group delay from its value at the center of the image for each of the four fringe patterns. The linear fringe pattern's group delay, \hat{N}_1 , varies linearly across the image with a range of $\pm 3\%$, in agreement with the expectations from the Veiras equation. However, the pixelated fringe pattern's group delay, \hat{N}_2 , varies by -8% to 2% , which is substantially larger than the expected $\pm 0.1\%$ variation. Moreover, the expected shape of \hat{N}_2 is a hyperbola, while the measured shape is an asymmetric hyperbolic fringe. This disagreement is suspected

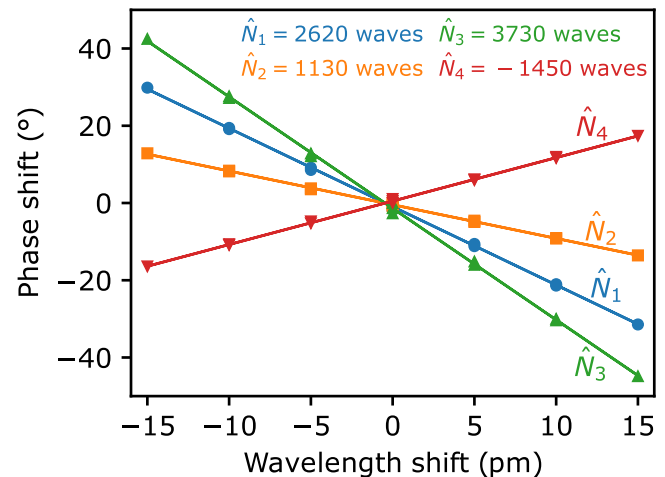


FIG. 3. Measured phase response at the center of the image for the four multi-delay fringe patterns during a ± 15 pm laser scan centered at the C III 465 nm line. The slope of each line gives the group delay \hat{N} for that fringe pattern.

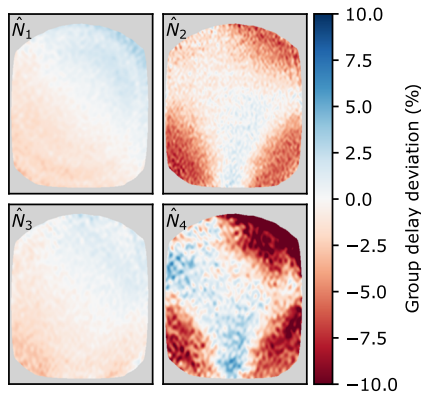


FIG. 4. Variation of group delay across the image for each of the four multi-delay fringe patterns. Each image displays the percent deviation of the group delay from its center value: $\hat{N}_{\text{deviation}} = 100\% \times (\hat{N} - \hat{N}_{\text{center}}) / \hat{N}_{\text{center}}$. Data in the gray region near the image boundary are masked due to vignetting of the calibration light source.

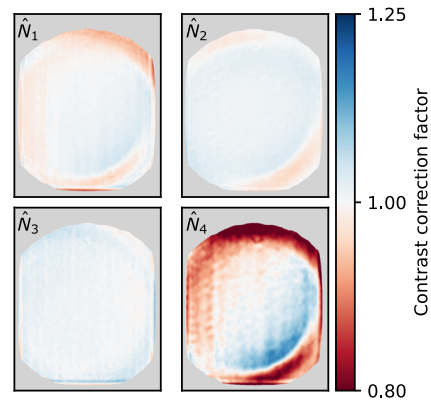


FIG. 5. 2D correction factor applied to the calibration contrast for each of the four multi-delay fringe patterns. This factor is needed to account for differences in the way that plasma light and calibration light are vignetted by the CIS optics. Data in the gray region near the image boundary are masked due to vignetting of the calibration light source.

to be due to a slight misalignment of the delay plate that was undetectable during assembly. (The laser scan measurements of \hat{N} were performed after the diagnostic was moved from the lab into the W7-X torus hall, upon which it became infeasible to adjust the alignment). Since the CIS data are analyzed using the measured 2D group delay, instead of an image center value or a theoretically calculated value, the results are unaffected by this kind of small misalignment.

The centroid phase Φ_0 and instrument contrast ζ_1 are measured immediately before and after every plasma discharge using the calibration laser. While Φ_0 is extremely sensitive to ambient temperature and varies appreciably between calibrations, ζ_1 is largely insensitive to temperature and is consistent between calibrations. The instrument contrast differs between the four fringe patterns; the average values in the central region of the image are $\zeta_{1,1} = 0.74$, $\zeta_{1,2} = 0.79$, $\zeta_{1,3} = 0.88$, and $\zeta_{1,4} = 0.38$. The instrument contrasts of the first two fringe patterns ($\zeta_{1,1}$ and $\zeta_{1,2}$), which each arise from a single crystal, are in line with the values achieved with the existing W7-X single-delay CIS instruments.⁷ The instrument contrast of the fringe pattern formed by the sum of the phase delays from both crystals ($\zeta_{1,3}$) is the highest. This result is counter-intuitive, as it might naively be expected that the instrument contrast decreases with the number of crystals as the surface flatness errors and refractive index inhomogeneities of each crystal add up. The instrument contrast of the fringe pattern formed by the difference of the phase delays from both crystals ($\zeta_{1,4}$) is substantially smaller than all the other ζ_1 values. It is possible that the imperfections of each crystal may partially cancel each other when forming $\zeta_{1,3}$, while adding constructively when forming $\zeta_{1,4}$, but we defer a detailed investigation into this to future work.

The centroid phase and instrument contrast determined with the calibration system differ from the true values that apply to plasma images due to a difference in the way the CIS optics vignette plasma light vs calibration light. This difference arises because plasma light is coupled into the CIS optics with an imaging fiber bundle, while calibration light is coupled with an integrating sphere and mirror,⁷ producing different light cones through the CIS optics for each source. Light cones with different angular spread illuminate

different portions of the crystal aperture, which produces a phase and contrast difference due to refractive index inhomogeneities and surface errors across the crystal aperture.¹¹ To correct this, phase and contrast measurements were taken with the calibration laser light coupled into the CIS optics using the fiber bundle that normally guides plasma light. The difference (ratio) of this phase(contrast) with respect to the value obtained with the same laser light coupled as normal through the calibration system gives a 2D phase(contrast) correction factor $\Phi_{\text{corr}}(\zeta_{\text{corr}})$. The true centroid phase and instrument contrast values to be used for analyzing plasma data are then calculated from the calibration values, Φ_{cal} and ζ_{cal} , measured for each plasma discharge using

$$\Phi_0 = \Phi_{\text{cal}} + \Phi_{\text{corr}}, \quad (19)$$

$$\zeta_1 = \zeta_{\text{cal}} \zeta_{\text{corr}}. \quad (20)$$

Figure 5 shows ζ_{corr} for each of the four multi-delay fringe patterns. Near the center of the image, the correction is small, i.e., $\zeta_{\text{corr}} \approx 1$. Moving toward the boundary of the image, ζ_{corr} increasingly deviates from 1, as the difference in vignetting of light introduced with the fiber bundle vs the calibration system becomes larger. The small-spatial-scale fluctuations of ζ_{corr} reflect demodulation error (see Sec. V A), which is the dominant source of uncertainty in the T_1 analysis. The fringe pattern encoded at \hat{N}_4 requires the most substantial correction, so the phase and contrast data extracted from this pattern have higher uncertainty than the data from the other patterns. The spatial structure and relative magnitudes of ζ_{corr} are similar for Φ_{corr} .

V. T_1 INFERENCE FROM MULTI-DELAY CIS DATA

A. Demodulation

Raw CIS images are dark-image subtracted and then demodulated to obtain the intensity, phase, and contrast encoded at each of the four group delays. This is carried out using a combination of Fourier transform demodulation and synchronous

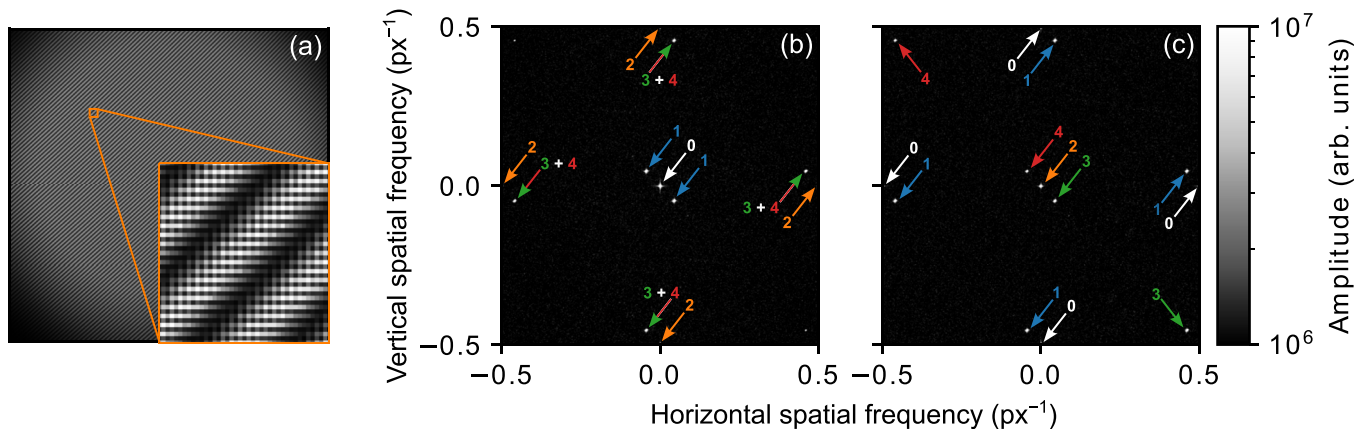


FIG. 6. (a) Calibration image taken with the multi-delay CIS instrument and zoomed-in inset showing the linear and pixelated fringe patterns. Spatial frequency spectra of (b) the calibration image and (c) the calibration image multiplied by the pixelated carrier phase. The peaks in the amplitude spectra correspond to different multi-delay fringe patterns and are labeled using the same numbering/color convention in Fig. 3 (0: mean intensity, 1: linear fringes, 2: pixelated fringes, 3: fringes due to sum of linear and pixelated group delays, and 4: fringes due to difference between linear and pixelated group delays).

demodulation.^{35,36} The spatial frequency spectrum of the image is first computed using a 2D discrete Fourier transform. An example CIS image is shown in Fig. 6(a), and the corresponding frequency spectrum is shown in Fig. 6(b). The peak with zero spatial frequency (center of the spectrum, white) corresponds to the mean image intensity, and the nearby peaks (blue) correspond to the linear fringe pattern. Each peak is filtered using a box-shaped fourth order Gaussian window function and then inverse Fourier transformed. For the center peak, this directly yields the intensity. For the linear fringe peak, this yields a complex analytic image whose argument and magnitude must be taken to obtain the phase and contrast of the linear fringe pattern.

This demodulation technique does not work for the remaining three fringe patterns because the pixelated fringe peaks (orange) are at the Nyquist frequencies, and the two mixed fringe patterns have overlapping peaks (green and red). These fringe patterns are demodulated using synchronous demodulation,³⁶ in which the image is first multiplied by the carrier phase of the pixelated fringe pattern before computing the frequency spectrum. The pixelated carrier phase is the phase delay induced by the quarter-wave plate and polarization camera. It is given by $\exp[i2\theta_p]$, where θ_p is the angle of the micropolarizer in front of each pixel on the polarization camera.³⁵ Multiplying the image by the pixelated carrier phase splits and shifts each peak in the frequency spectrum [Fig. 6(c)] by 0.5 px^{-1} horizontally and vertically [see Eq. (4.148) in Ref. 36]. This separates the two mixed fringe patterns and moves them, along with the pixelated fringe pattern, to the center of the spectrum. They are then filtered and inverse Fourier transformed in the same fashion as the linear fringe peak.

Demodulation errors in the intensity, phase, and contrast arise from leakage of spectral content from one peak into the filter box of a different peak. Due to discontinuity at the rectangular boundary of the image, spectral leakage primarily occurs in the horizontal and vertical directions, manifesting as cross-shaped peaks in the frequency spectrum. To mitigate this, the optical components are aligned to produce 45° tilted linear fringes, which causes the peaks in the frequency spectrum to be diagonally separated. Spectral leakage

is also caused by the discrete, grid-like nature of the individual fibers composing the imaging fiber bundle, which introduces high-spatial-frequency components into the spectrum. This form of spectral leakage is suppressed by defocusing the collimating lens to blur the individual fibers, which reduces the spatial resolution from $\sim 1 \text{ mm}$ to $\sim 1 \text{ cm}$.

While not a source of spectral leakage, image noise from photon and readout noise also produces errors in demodulated quantities. Image noise is distributed broadly across the frequency spectrum, so decreasing the size of the filter boxes reduces the amount of noise-induced demodulation error. The optimal filter box size is then the smallest box that includes the full spectral content of the peak. Images taken during periods of stationary plasma conditions can be averaged together to suppress noise, but time-averaging has no effect on the demodulation errors caused by spectral leakage. Since W7-X plasmas often include stationary periods lasting multiple seconds, time-averaging can frequently be employed. Therefore, the dominant source of uncertainty is usually spectral-leakage-induced demodulation error.

Demodulation errors appear as small-spatial-scale fluctuations in the intensity, phase, and contrast. Uncertainties of these quantities are then estimated by computing the root-mean-square average amplitude of these fluctuations across the demodulated image. For cases where spectral leakage is the main source of uncertainty, the phase and contrast uncertainties estimated with this method are about 2° and 2%, respectively.

B. Fitting model

To infer T_i and other plasma parameters, a model for the phase and contrast is fit to the demodulated data using the `scipy.optimize.curve_fit` non-linear least squares routine.³⁷ The model assumes that the C III line shape is governed exclusively by the Doppler and Zeeman effects and is given by simplified versions of Eqs. (4) and (5). Stark broadening is negligible for the C III line, and background emission is assumed to be small compared to line radiation (in Sec. VI, this assumption is verified using spectrometer measurements).

In general, the C III emission is distributed along the sightline for each pixel, and the measured phase and contrast reflect emissivity-weighted, line-averaged values.³⁸ However, previous high-resolution spectrometer measurements^{6,8} and tomographic inversions of the C III radiation distribution³⁹ have shown that it is largely localized to bands that are a few centimeters wide due to the narrow T_e range for which emission occurs (see Sec. III A). Therefore, the fitting model assumes that the emission is localized somewhere along the sightline for each pixel.

The sightline vector for each pixel is determined from a geometric camera calibration performed using Calcam.⁴⁰ W7-X is optimized to have low net toroidal plasma current,^{41,42} so B is generated predominantly from external magnets and can be calculated with high accuracy throughout the plasma.⁴³ Figure 7 shows the CIS field of view and the variation of B and α along four example sightlines that view different plasma-facing components in W7-X. All sightlines first pass through a 20 cm thick region of the SOL (the first red-shaded region) that is in a gap between divertor targets, then through the hot core plasma, and finally through a 20–50 cm thick region of the SOL (the second red-shaded region) near divertor targets. C III radiation mostly comes from the second SOL region owing to its proximity to the carbon source at the divertors.

The line shape model has four fit parameters: ion temperature T_i , line-of-sight-directed ion velocity v_i , magnetic field B , and field-sightline angle α at the emission location. Since B and α are known along every sightline, these two parameters can be replaced by a single parameter: the distance along the sightline of the C III emission location. CIS is thus capable, in principle, of providing radiation location measurements in addition to T_i and v_i . Plasma parameter inference is performed by fitting a model with three parameters to eight data points (four contrasts and four phases). This fit is performed independently for every pixel in the image. Uncertainties in the fit parameters are produced automatically by the fitting routine based on the input phase and contrast uncertainties.

VI. VALIDATION OF SOL T_i MEASUREMENTS ON W7-X

A. Experimental setup

We now validate the multi-delay CIS instrument's ability to infer T_i by comparing its measurements in W7-X plasmas to those from a high-resolution spectrometer. The spectrometer has previously been used to derive impurity ion temperatures from the spectra of several impurity emission lines,⁶ including the C III 465 nm line observed by CIS. About half of the spectrometer channels are connected via 70–100 m long optical fibers to a set of plasma facing optics that are located in the same port only a few centimeters away from the CIS plasma facing lens. The fibers are arranged in a linear fan of 27 sightlines that overlap the CIS field of view [indicated by the white dots shown in Fig. 8(a)], allowing for a direct comparison between the two diagnostics.

To perform as precise a comparison as possible, we use a stationary 100 s long-pulse W7-X plasma (discharge ID 20230215.015). The plasma has a line-averaged density of $3.8 \times 10^{19} \text{ m}^{-3}$ and is heated by 3.3 MW of electron cyclotron resonance power. The edge plasma is attached to the divertor and is in a limiter-like configuration where the edge islands have moved inside the last closed flux surface.⁴⁴ During the first 40 s, the edge plasma parameters vary as the toroidal current evolves to its equilibrium value of 10.5 kA, so

CIS and the spectrometer are compared over the 40–100 s time window, for which all plasma parameters are stationary. The 60 s long time-averaging window greatly reduces the uncertainty of the spectrometer data (2 s exposure time), which is normally substantially higher than that of the CIS data due to the spectrometer's lower optical throughput. The CIS data uncertainties are only modestly reduced by time-averaging because the main source of uncertainty is spectral-leakage-induced demodulation error, which is consistent from image to image.

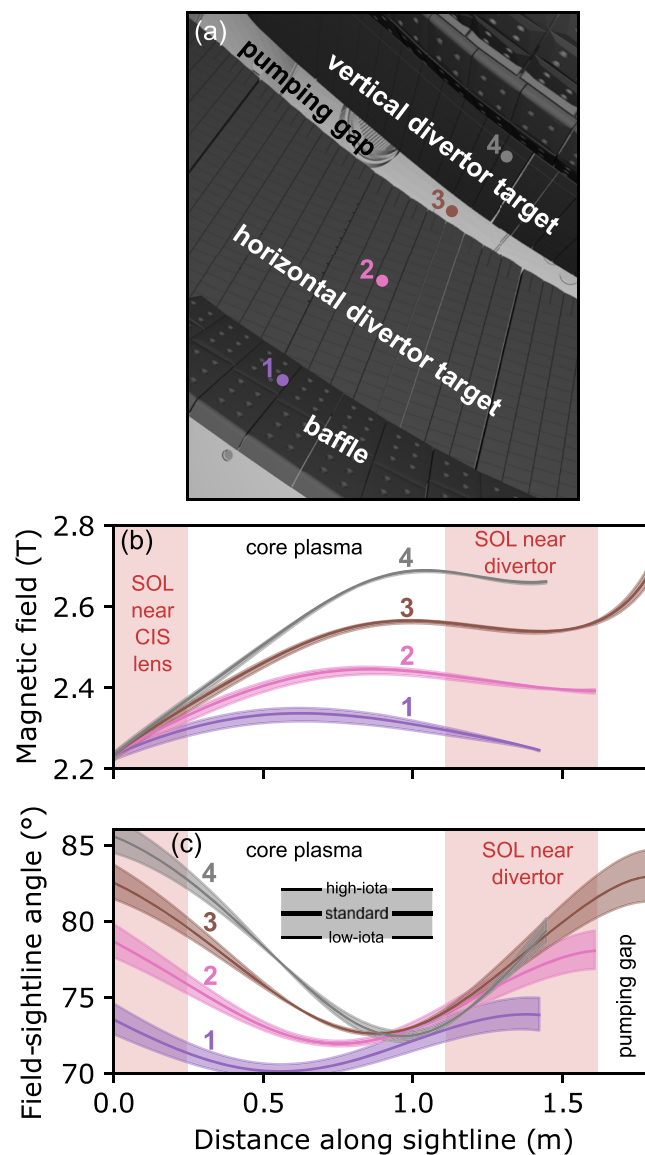


FIG. 7. (a) CIS camera field of view with four example sightlines marked by the colored dots. Variation of (b) magnetic field strength B and (c) angle between magnetic field and camera sightline α along the four example sightlines. Colored bands around each trace show how much B and α vary between the W7-X standard, low-iota, and high-iota magnetic configurations. The light red-shaded regions denote the portions of the sightlines within the scrape-off layer (SOL) plasma.

Figure 8 shows the CIS observations averaged over the 60 s time window. The C III radiation intensity [Fig. 8(a)] exhibits several toroidally elongated emission bands: one intense band near the vertical target and four dimmer bands near the horizontal target. The contrast images encoded at each of the four group delays [Fig. 8(b)] have similar toroidally elongated structures, and the overall contrast level in each image is noticeably different, in line with the expectations based on the fine structure of the C III 465 nm line [see Fig. 1(b)]. Figure 8 also shows the locations of the overlapping spectrometer sightlines by the white dots, which span across three of the horizontal target radiation bands and the vertical target radiation band. All the overlapping sightlines of the spectrometer used in this comparison are labeled with even numbers, going

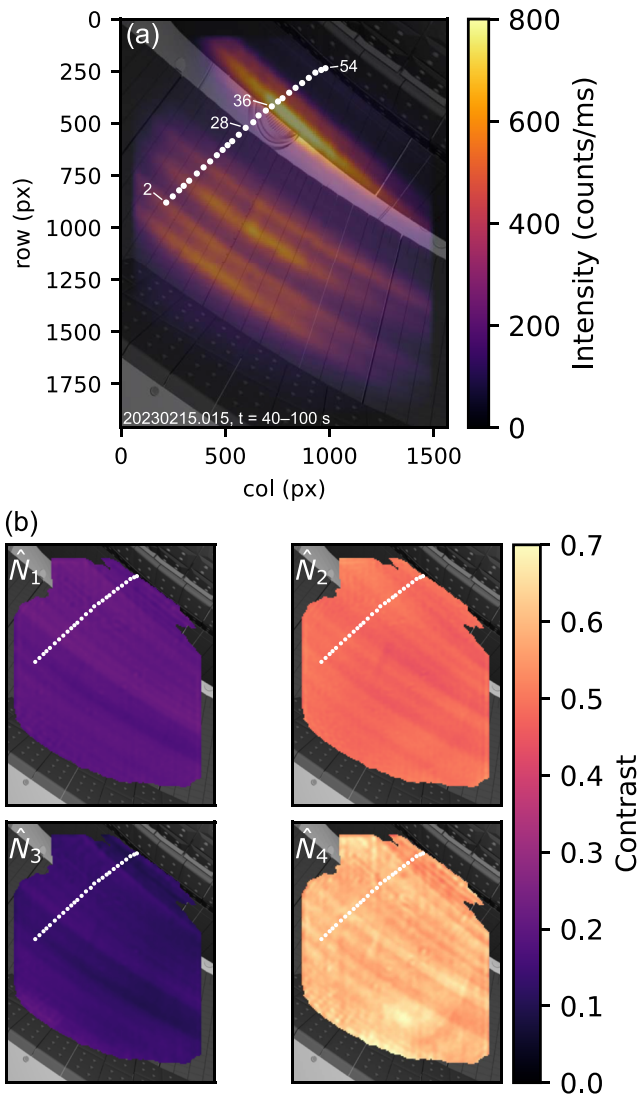


FIG. 8. CIS measurements in a long-pulse W7-X plasma of (a) C III radiation intensity and (b) contrast encoded at each of the four group delays. The locations of the high-resolution spectrometer sightlines are marked by the white dots.

from sightline 2 on the horizontal target up to sightline 54 at the top of the vertical target. The fibers connected to sightlines 20 and 34 are damaged, so no spectrometer data are shown for these sightlines.

B. Comparison between CIS and spectrometer spectra

Figure 9 compares the spectrometer and CIS spectral measurements at three select sightlines. Sightline 38 [Figs. 9(a) and 9(d)] has the highest signal of all sightlines and is, therefore, expected to be the best for comparison. In contrast, sightlines 44 [Figs. 9(b) and 9(e)] and 26 [Figs. 9(c) and 9(f)] are more stringent comparison cases because sightline 44 shows the strongest evidence of spectral contamination within the C III multiplet, and sightline 26 has the lowest signal-to-noise ratio. The spectrometer wavelength spectra, displayed as blue traces in the top row [Figs. 9(a)–9(c)], are not directly comparable with the CIS contrast data, shown by the black dots in the bottom row [Figs. 9(d)–9(f)]. To directly compare the two diagnostics, the wavelength spectrum $I(\lambda)$ for each sightline is Fourier transformed to calculate an equivalent contrast vs group delay spectrum,

$$\zeta(\dot{N}) = \frac{1}{I_0} \left| \int I(\lambda) \exp[-2\pi i \dot{N} \lambda / \lambda_0] d\lambda \right|, \quad (21)$$

where I_0 is the integrated spectral intensity. These equivalent contrast spectra are represented in the bottom row of Fig. 9 by the blue traces. Note that these traces are largely overlapped by the orange fits to the data.

For all three example sightlines, the difference between the CIS contrast and the equivalent spectrometer contrast is within the errorbars of the CIS data. CIS phase and contrast uncertainties are estimated using the method described in Sec. V A, which are then propagated to obtain uncertainties for the group delay and calibration correction factors described in Sec. IV. The errorbars for both the group delay and contrast are a few percent and are comparable to the size of the plotted data points, with the exception of the contrast encoded at $\dot{N}_4 = 1450$ waves, which has a higher uncertainty because it has the lowest instrument contrast and requires the largest calibration correction (see Sec. IV). The spectrometer data errorbars are substantially smaller than those for CIS due to the long time-averaging window and are too small to be visible. Figures 9(d)–9(f) thus shows close agreement between the contrast data from each diagnostic, verifying that they both collect light with equivalent spectral information and validating the demodulation procedure used to extract contrast from multi-delay CIS interference patterns. Similarly, close agreement of the contrast data are observed for all other sightlines.

The spectrometer wavelength spectra are fitted with the same line shape model as CIS (see Sec. V B), and the fits are displayed as orange traces in the top row of Fig. 9. In contrast to previous fits of W7-X C III spectra,^{6,8} it is found here that the intensities of the $J = 0$ and $J = 1$ components of the C III triplet need to be scaled upward by 15% compared to the values for a statistical population distribution. A similar scaling factor was needed to fit C III spectra in the TEXTOR tokamak and was found to range from 0.85 under plasma conditions with strong recombination, which

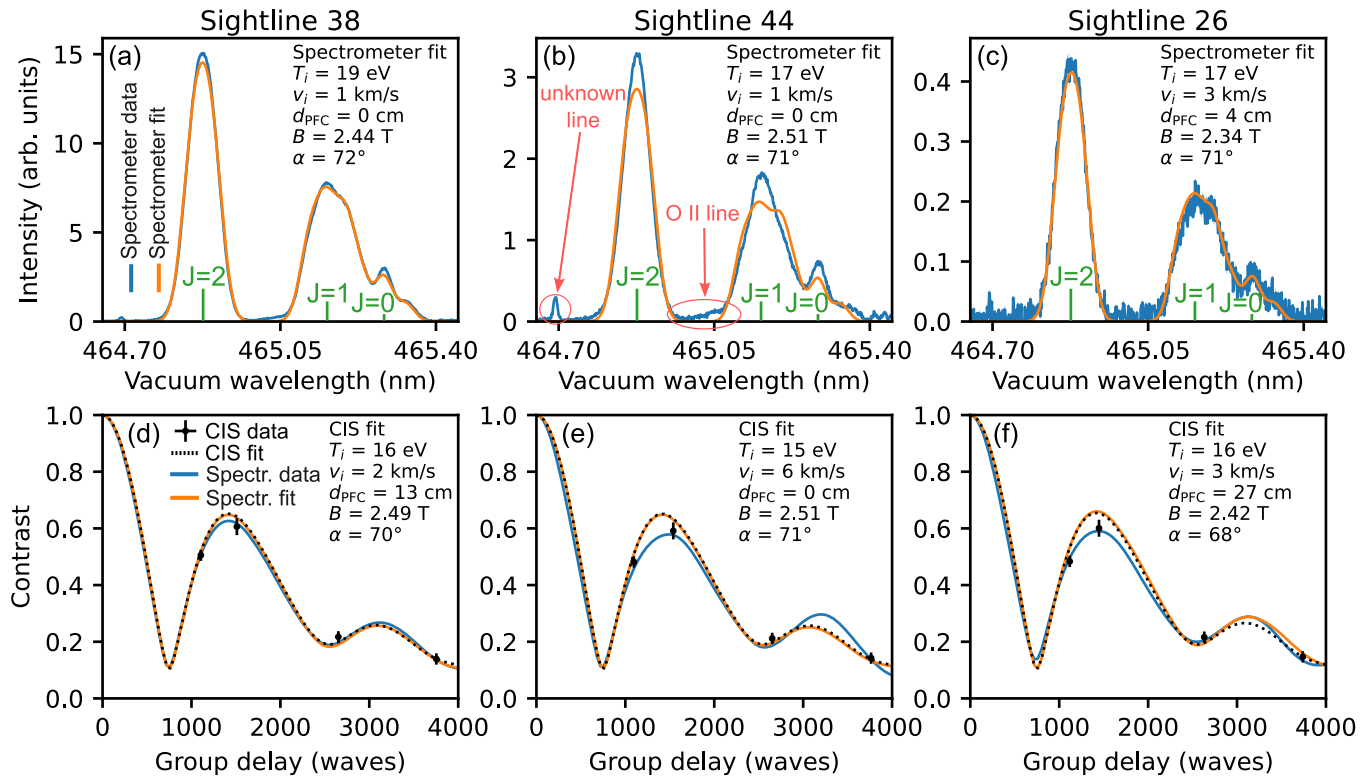


FIG. 9. Comparison between CIS and high-resolution spectrometer measurements for select sightlines. Top row: spectrometer wavelength spectra (blue) and fits to the spectra (orange). Bottom row: CIS contrast at each of the four group delays (black points), fits to the CIS contrast (black dashed line), equivalent contrast curves of the spectrometer wavelength spectra (blue), and contrast curves of the spectrometer fits (orange). The three fine-structure components of the C III triplet are marked by the green lines. Sightline 38 [(a) and (d)] observes intense C III radiation from the vertical target strike line and exhibits the best agreement between the two diagnostics and their fits. Sightline 44 [(b) and (e)] shows the lowest spectrometer fit quality. Sightline 26 [(c) and (f)] has the noisiest spectrum but still shows relatively good agreement.

08 July 2024 14:04:22

preferentially populates upper J levels, to 1.15 under plasma conditions with strong electron impact excitation, which preferentially populates lower J levels.³² The scaling factor of 1.15 found here presumably arises because in this attached plasma, the carbon atoms sputtered from the divertor are rapidly ionized through successively higher charge states, and during the period they exist in the C^{2+} state, electron collisions populate the excited states on a time scale faster than ion-ion collisions can relax the excited state population to its statistical distribution.

The fit quality to the spectrometer data is generally good across most sightlines, including both high-signal [Fig. 9(a)] and low-signal [Fig. 9(c)] sightlines. However, the fit quality is noticeably lower for sightline 44 [Fig. 9(b)] and those immediately around it. These sightlines show evidence of spectral contamination by an O II line at 465.04 nm and an unknown line at 464.69 nm, but the intensity of these contamination lines relative to the C III line is 4%, so they have little impact on the fits. Rather, the cause of the reduced fit quality appears to be a discrepancy between the model and data on the blue flank of the $J = 1$ component. The model exhibits a small secondary peak on this flank created by overlapping Zeeman components, while the data exhibit a single narrow peak. This discrepancy might be caused by spectral contamination from an unknown line

near the $J = 1$ component, inaccuracy of the sightline spatial calibration near the vertical target, or the existence of multiple C III emission zones along the sightline.

The equivalent contrast of the fit to each wavelength spectrum (orange curve) is compared against the fit to the CIS data (black dashed curve) in the bottom row of Fig. 9. For sightline 38 [Fig. 9(d)], the two fits nearly overlap, demonstrating quite close agreement for a sightline with high signal. The two fits also agree closely for sightline 44 [Fig. 9(e)], indicating that the discrepancy between the line shape model and the data for this sightline affects both diagnostics similarly. For sightline 26 [Fig. 9(f)], where the signal-to-noise is lowest, the fits slightly deviate from each other in the $\tilde{N} = 3000$ –3800 waves range but are otherwise in close agreement. The overall good agreement between the fits to the CIS and spectrometer data validates the fitting procedure.

C. Comparison between CIS and spectrometer inferred parameters

Figure 10 compares plasma parameters inferred independently from CIS and the spectrometer for all overlapping sightlines. Since the two diagnostics have substantially different optical throughput,

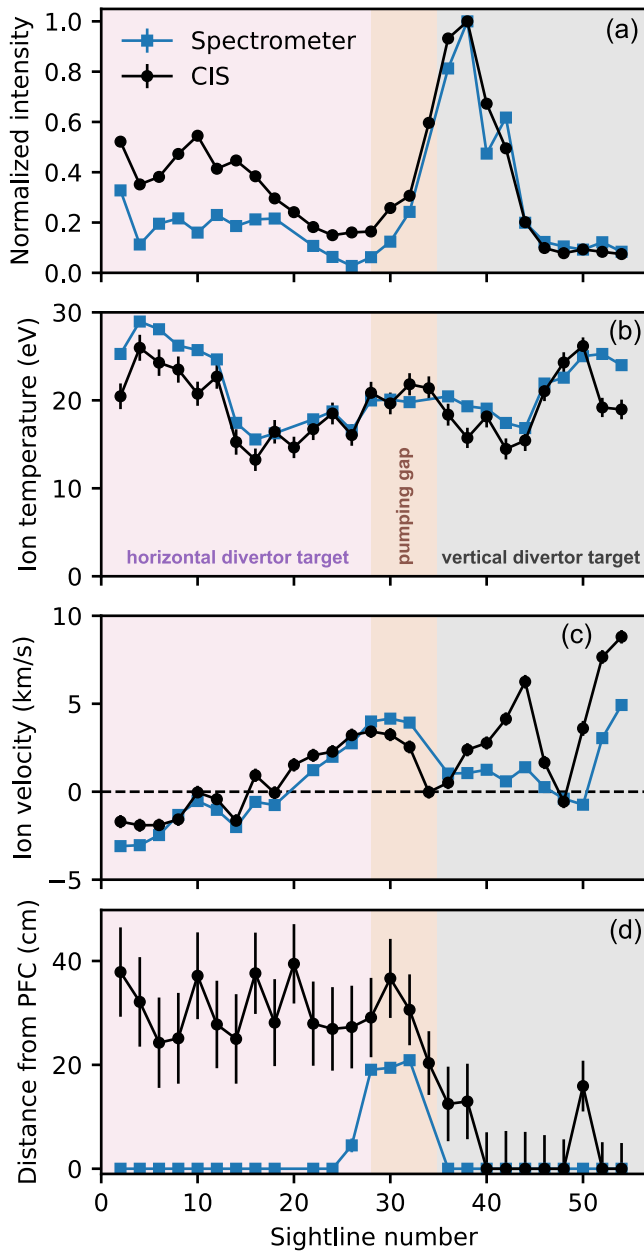


FIG. 10. Comparison across all sightlines of CIS- and spectrometer-inferred (a) C III intensity, (b) C^{2+} ion temperature, (c) C^{2+} ion velocity along sightline, and (d) distance of the C III emission band from the plasma facing component viewed by the sightline. The C III intensity for each diagnostic is normalized by its peak value. The shaded regions denote the plasma facing components observed by each sightline.

the C III intensity [Fig. 10(a)] for each diagnostic is normalized by its peak value, which occurs at sightline 38. The profiles of the C III intensity have similar shapes, with CIS having somewhat higher intensity for sightlines 2–30, which view the horizontal divertor. This deviation is likely caused by differences in vignetting by the

plasma facing lens for each diagnostic and/or the lack of absolute intensity calibrations.

Figure 10(b) shows that C^{2+} ion temperatures inferred from CIS and the spectrometer are in remarkably good agreement across nearly all sightlines. On average, the T_i difference is 2.2 eV (or 10%), and the largest difference is 5 eV (25%) for the sightlines at the ends of the array. The T_i profile shapes are quite similar, with both diagnostics observing an increase in sightlines 2–12, viewing the middle of the horizontal divertor, and sightlines 46–50, viewing the upper part of the vertical divertor. The intensity of the O II contamination line ranges from 2% to 4% of the C III intensity across the sightlines and has little influence on the inferred T_i . This is evidenced by the good T_i agreement at sightline 44, which has the most O II contamination. The presence of background emission also has little effect on T_i , as the signal-to-background ratio is ~ 30 , causing only a $\approx 3\%$ reduction of the CIS contrast.

As discussed in Sec. VI B, the amplitudes of the $J = 0$ and $J = 1$ components of the C III triplet have to be scaled upward by 15% relative to their statistical values to fit the CIS and spectrometer data. Adjusting the amplitudes of these components has a negligible impact on the T_i values inferred from the spectrometer data but *does* affect the CIS T_i . Using statistical amplitudes when fitting CIS data yield T_i values $\approx 30\%$ higher than those obtained with the scaled amplitudes. The optimal scaling factor for the $J = 0$ and $J = 1$ triplet components is consistently 1.15 across all sightlines for the long-pulse attached plasma analyzed in detail here. However, this scaling factor can change with plasma conditions. In particular, it is observed to be one in detached plasmas, i.e., in detached plasmas, the C III triplet component amplitudes follow the statistical distribution.

Since CIS does not obtain enough spectral information to determine the scaling factor, it must be extracted from spectrometer measurements. This breaks the independence of CIS and the spectrometer. Future SOL physics investigations with this CIS instrument will first use the spectrometer to characterize the dependence of the scaling factor on the main W7-X control parameters: line-averaged density, heating power, and radiated power fraction. For discharges without spectrometer data, an uncertainty on T_i can be determined by fitting the data with both extremes of the scaling factor: 0.85 at minimum and 1.15 at maximum. For the long-pulse W7-X plasma analyzed here, this uncertainty would be $\pm 30\%$.

Figure 10(c) compares the sightline-projected C^{2+} ion velocity from CIS and the spectrometer. The v_i profiles agree within $\pm 1.5 \text{ km s}^{-1}$ over the horizontal target and pumping gap, while over the vertical target, they deviate by up to 5 km s^{-1} . This deviation is correlated with the region where there is a discrepancy between the C III line shape model and the spectrometer data [Fig. 9(b)]. This discrepancy does not adversely affect the spectrometer-inferred v_i because only the $J = 1$ component is affected, so the Doppler shift can still be readily extracted from the positions of the $J = 0$ and $J = 2$ components. However, it does affect the CIS-inferred v_i because modification of the line shape effectively alters the multiplet phase. Interestingly, the CIS T_i appears to be unaffected by this line shape model inaccuracy, as the CIS- and spectrometer-inferred T_i values agree well over the vertical target. Overall, this comparison demonstrates that optimizing a CIS diagnostic for ion temperature measurements does not degrade the ability to measure ion velocity, provided an accurate line shape model is available.

Figure 10(d) reveals a major discrepancy between the CIS- and spectrometer-inferred locations of the C III emission band. The spectrometer finds that C III radiates right at the divertor target, except for sightlines 28–34, where the radiation is at the pumping gap entrance between the horizontal and vertical divertors (note that the distance from the pumping gap entrance to the vacuum vessel is about 20 cm). This is the expected behavior in attached plasmas and is in agreement with previous tomographic reconstructions of the C III radiation distribution.³⁹ In contrast, CIS infers the C III emission location to be 25–40 cm away from the horizontal divertor, which would put the radiation inside the last closed flux surface and is, therefore, unphysical. The inability of CIS to determine the radiation location is a result of the T_i -optimization of the instrument's crystal. Radiation localization is tied to the magnetic field variation along a sightline, and therefore, it depends on the instrument's sensitivity to Zeeman splitting. The crystal is designed to have minimal sensitivity to Zeeman splitting to improve the accuracy of the inferred T_i , which then diminishes the accuracy of the inferred emission location.

D. Imaging the divertor T_i distribution

Having now validated the CIS T_i measurements against those of the high-resolution spectrometer at the two diagnostics' overlapping sightlines, Fig. 11 displays T_i over the entire CIS field of view. The T_i distribution exhibits toroidally elongated structures aligned with the C III emission bands shown in Fig. 8(a) and ranges between 12 and 35 eV across the image. T_i appears to be inversely correlated with C III radiation intensity: the band of the highest T_i on the horizontal divertor is located in the gap between emission bands, while the intense band on the vertical divertor has among the lowest T_i across the image. There is also a tendency for T_i to increase moving toroidally away from the plasma-material interaction zone (moving down and to the right in the image). The wealth of spatial information in Fig. 11 demonstrates the utility of imaging the T_i distribution in the divertor of a fully 3D SOL.

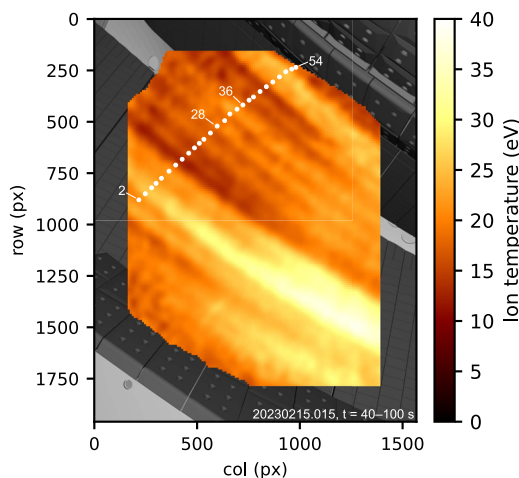


FIG. 11. CIS-inferred C^{2+} ion temperature in a long-pulse W7-X plasma. The locations of the high-resolution spectrometer sightlines are marked by the white dots.

VII. SUMMARY AND DISCUSSION

We have designed, built, and experimentally validated a new coherence imaging spectroscopy instrument optimized to measure ion temperatures in the divertor of the W7-X stellarator. Historically, T_i measurements in this domain have been challenging due to the need to deconvolve the effects of Doppler broadening and Zeeman splitting on the line shape. This problem is solved by (1) using a recently developed multi-delay CIS configuration³⁵ to obtain four times the spectral information as conventional CIS and (2) using a novel approach to birefringent crystal design to minimize the instrument's sensitivity to Zeeman splitting. While the CIS diagnostic described here is optimized specifically for C^{2+} ion temperature measurements in the SOL of W7-X, the design approach described in this work is more broadly applicable to any magnetically confined plasma with multi-tesla field strengths and ion temperatures on the order of 10 eV.

The T_i -optimized CIS diagnostic is extensively characterized using a precision tunable laser and validated on W7-X by comparison with a high-resolution dispersive spectrometer. The spectrometer sightlines overlap with the CIS field of view, so both diagnostics collect nearly identical light, allowing a direct comparison. Excellent agreement between CIS and the spectrometer is observed for both the spectra and inferred T_i values. The spectrometer data indicate the presence of background emission and spectral contamination, but these non-ideal features are small enough that they have little effect on the inferred T_i . The comparison performed in this work focuses on a single long-pulse W7-X plasma to maximize the signal-to-noise ratio of the spectrometer data. However, CIS operated routinely throughout the entirety of the recently completed OP2.1 experimental campaign, so there is a substantial archive of T_i data to be used for future investigations of scrape-off layer physics.

A major goal of this work is to develop the capability for CIS to measure T_i independently of other diagnostics. This builds off previous results where CIS T_i measurements were made by cross-calibrating the CIS data with the high-resolution spectrometer.⁸ This goal is not completely achieved here because it is found that the C III triplet component amplitudes vary with plasma parameters. Accurately extracting T_i from CIS data then requires these relative amplitudes to first be determined from the spectrometer data. Nevertheless, this work still makes substantial progress toward the goal of independent T_i measurements, as the previous approach of using a spectrometer to cross-calibrate CIS only yields accurate T_i in the vicinity of the shared sightlines. In contrast, the CIS instrument developed here retains the ability to accurately infer T_i across the entire field of view. In addition, in cases where the triplet component amplitudes are not available, the systematic uncertainty in the inferred T_i is $\approx 30\%$, which may be acceptably small depending on the type of physics investigation the T_i data are being used for.

The design of this CIS instrument is solely focused on accurately measuring T_i , motivating the specification of a crystal with minimized sensitivity to Zeeman splitting. CIS is also, in principle, capable of determining the location of C III emission since the magnetic field is known to high precision inside low- β , low-net-current W7-X plasmas. However, the crystal optimization employed here makes the instrument so insensitive to Zeeman splitting that

it is unable to accurately determine the emission location. A future multi-delay CIS diagnostic with the existing crystal having minimal sensitivity to Zeeman splitting, plus a new crystal designed for *maximal* sensitivity to Zeeman splitting, is being investigated to allow simultaneous T_i and C III radiation localization measurements in W7-X.

ACKNOWLEDGMENTS

We thank Saikat Chakraborty Thakur, Cameron Royer, Tomas Gonda, Eleanor Williamson, and Edward Thomas Jr. for helping perform an experiment on the Magnetized Dusty Plasma Experiment (MDPX)⁴⁵ that tested a prototype of the multi-delay CIS instrument. We also thank Curt Johnson for discussions on Zeeman splitting and Oliver Ford for help in implementing the data acquisition. This work has been supported by the US DoE Grant No. DE-SC0014529. This work has been carried out within the framework of the EUROfusion Consortium, funded by the European Union via the Euratom Research and Training Programme (Grant Agreement No. 101052200—EUROfusion). Views and opinions expressed are, however, those of the author(s) only and do not necessarily reflect those of the European Union or the European Commission. Neither the European Union nor the European Commission can be held responsible for them.

AUTHOR DECLARATIONS

Conflict of Interest

The authors have no conflicts to disclose.

Author Contributions

David M. Kriete: Conceptualization (equal); Data curation (lead); Formal analysis (lead); Investigation (equal); Methodology (lead); Project administration (lead); Resources (equal); Software (lead); Validation (lead); Visualization (lead); Writing – original draft (lead); Writing – review & editing (lead). **Valeria Perseo:** Conceptualization (equal); Data curation (supporting); Formal analysis (supporting); Investigation (equal); Methodology (supporting); Project administration (equal); Resources (lead); Software (supporting); Validation (equal); Visualization (supporting); Writing – review & editing (equal). **Dorothea Gradic:** Conceptualization (equal); Data curation (supporting); Formal analysis (supporting); Investigation (equal); Methodology (supporting); Resources (equal); Software (supporting); Validation (equal); Writing – review & editing (equal). **David A. Ennis:** Conceptualization (equal); Funding acquisition (equal); Investigation (supporting); Project administration (equal); Resources (supporting); Supervision (equal); Writing – review & editing (equal). **Ralf König:** Conceptualization (equal); Funding acquisition (equal); Resources (supporting); Supervision (supporting); Writing – review & editing (supporting). **David A. Maurer:** Conceptualization (equal); Funding acquisition (equal); Project administration (supporting); Supervision (supporting); Writing – review & editing (supporting).

DATA AVAILABILITY

The data that support the findings of this study are openly available in the Auburn University Repository of Research Activities (AUrora) at <https://doi.org/10.35099/aurora-701>, Ref. 46.

REFERENCES

- ¹P. C. Stangeby, *The Plasma Boundary of Magnetic Fusion Devices*, *Plasma Physics Series* (Institute of Physics Publishing, Bristol ; Philadelphia, 2000).
- ²M. Kočan, J. Gunn, S. Carpentier-Chouchana, A. Herrmann, A. Kirk, M. Komm, H. Müller, J.-Y. Pascal, R. Pitts, V. Rohde, and P. Tamain, *J. Nucl. Mater.* **415**, S1133 (2011).
- ³G. F. Matthews, *Plasma Phys. Controlled Fusion* **36**, 1595 (1994).
- ⁴Y. Li, M. Henkel, Y. Liang, A. Knieps, P. Drews, C. Killer, D. Nicolai, J. Cosfeld, J. Geiger, Y. Feng, F. Effenberg, D. Zhang, P. Hacker, D. Höschen, G. Satheeswaran, S. Liu, O. Grulke, M. Jakubowski, S. Brezinsek, M. Otte, O. Neubauer, B. Schweer, G. Xu, J. Cai, Z. Huang, and the W7-X team, “Measurement of the edge ion temperature in W7-X with island divertor by a retarding field analyzer probe,” *Nucl. Fusion* **59**, 126002 (2019).
- ⁵M. Henkel, Y. Li, Y. Liang, P. Drews, A. Knieps, C. Killer, D. Nicolai, D. Höschen, J. Geiger, C. Xiao, N. Sandri, G. Satheeswaran, S. Liu, O. Grulke, M. Jakubowski, S. Brezinsek, M. Otte, O. Neubauer, B. Schweer, G. Xu, and J. Cai, *Fusion Eng. Des.* **157**, 111623 (2020).
- ⁶D. Gradic, M. Krychowiak, R. König, F. Henke, M. Otte, V. Perseo, and T. S. Pedersen, *Plasma Phys. Controlled Fusion* **64**, 075010 (2022).
- ⁷V. Perseo, D. Gradic, R. König, O. P. Ford, C. Killer, O. Grulke, D. A. Ennis, and W7-X Team, *Rev. Sci. Instrum.* **91**, 013501 (2020).
- ⁸D. Gradic, V. Perseo, D. Kriete, M. Krychowiak, R. König, Y. Feng, M. Otte, T. S. Pedersen, Y. Gao, M. Jakubowski, G. Schlisio, F. Warmer, and W7-X Team, “2D coherence imaging measurements of C²⁺ ion temperatures in the divertor of Wendelstein 7-X,” *Nucl. Fusion* **61**, 106041 (2021).
- ⁹J. Howard, *J. Phys. B: At., Mol. Opt. Phys.* **43**, 144010 (2010).
- ¹⁰C. Zhang, B. Zhao, and B. Xiangli, *Appl. Opt.* **43**, 6090 (2004).
- ¹¹S. A. Silburn, “A Doppler coherence imaging diagnostic for the mega-amp spherical tokamak,” Ph.D. thesis (Durham University, 2014).
- ¹²F. E. Veiras, L. I. Perez, and M. T. Garea, *Appl. Opt.* **49**, 2769 (2010).
- ¹³J. Howard, R. Jaspers, O. Lischtschenko, E. Delabie, and J. Chung, *Plasma Phys. Controlled Fusion* **52**, 125002 (2010).
- ¹⁴P. Urlings, “Multiple delay coherence imaging charge exchange recombination spectroscopy,” M.S. thesis (Eindhoven University of Technology, 2015).
- ¹⁵R. Lopez-Cansino, V. Perseo, E. Viezzer, D. M. Kriete, O. P. Ford, T. Romba, P. Z. Poloskei, and W7-X Team, *Plasma Phys. Controlled Fusion* **66**, 045012 (2024).
- ¹⁶J. D. Hey, C. C. Chu, and Ph. Mertens, *Contrib. Plasma Phys.* **42**, 635 (2004).
- ¹⁷J. D. Hey, C. C. Chu, P. Mertens, S. Brezinsek, and B. Unterberg, *J. Phys. B: At., Mol. Opt. Phys.* **37**, 2543 (2004).
- ¹⁸H. P. Summers, *The ADAS User Manual*, version 2.6 (2004).
- ¹⁹H. R. Griem, *Spectral Line Broadening by Plasmas* (Academic Press, New York, 1974).
- ²⁰J. Rosato, Y. Marandet, and R. Stamm, *J. Quant. Spectrosc. Radiat. Transfer* **187**, 333 (2017).
- ²¹O. Lischtschenko, K. Bystrov, G. De Temmerman, J. Howard, R. J. E. Jaspers, and R. König, *Rev. Sci. Instrum.* **81**, 10E521 (2010).
- ²²D. Gradic, V. Perseo, R. König, D. Ennis, and W7-X Team, *Fusion Eng. Des.* **146**, 995 (2019).
- ²³C. Samuelli, S. Allen, W. Meyer, and J. Howard, *J. Instrum.* **12**, C08016 (2017).
- ²⁴K. Ueda, M. Nishiura, N. Kenmochi, Z. Yoshida, and K. Nakamura, *Rev. Sci. Instrum.* **92**, 073501 (2021).
- ²⁵N. Allen, D. Ennis, S. Allen, C. Samuelli, D. Kriete, C. Johnson, G. Hartwell, and D. Maurer, *J. Instrum.* **18**, P06030 (2023).
- ²⁶J. S. Allcock, S. A. Silburn, R. M. Sharples, J. R. Harrison, N. J. Conway, T. Long, and N. Lin, *Opt. Express* **31**, 1901 (2023).
- ²⁷C. M. Samuelli, A. G. Mclean, S. L. Allen, M. E. Fenstermacher, C. J. Lasnier, G. D. Porter, T. D. Rognlien, F. Scotti, V. Soukhanovskii, W. H. Meyer, A. E. Jaervinen, A. Holm, M. Groth, D. A. Ennis, C. A. Johnson, F. Glass, H. Guo, A.

- W. Leonard, A. L. Moser, D. Thomas, H. Q. Wang, J. D. Watkins, J. Boedo, E. M. Hollmann, and R. S. Wilcox, in *28th IAEA Fusion Energy Conference* (IAEA, Vienna; Nice, France, 2021), p. IAEA-EX-P1/867.
- ²⁸C. Killer, O. Grulke, P. Drews, Y. Gao, M. Jakubowski, A. Knieps, D. Nicolai, H. Niemann, A. P. Sitjes, G. Satheeswaran, and W7-X Team, "Characterization of the W7-X scrape-off layer using reciprocating probes," *Nucl. Fusion* **59**, 086013 (2019).
- ²⁹Y. Feng, M. Jakubowski, R. König, M. Krychowiak, M. Otte, F. Reimold, D. Reiter, O. Schmitz, D. Zhang, C. Beidler, C. Biedermann, S. Bozhenkov, K. Brunner, A. Dinklage, P. Drewelow, F. Effenberg, M. Endler, G. Fuchert, Y. Gao, J. Geiger, K. Hammond, P. Helander, C. Killer, J. Knauer, T. Kremeyer, E. Pasch, L. Rudischhauser, G. Schlisio, T. Sunn Pedersen, U. Wenzel, V. Winters, and W7-X Team, "Understanding detachment of the W7-X island divertor," *Nucl. Fusion* **61**, 086012 (2021).
- ³⁰T. Sunn Pedersen, T. Szepesi, R. König, F. Reimold, D. Zhang, G. Fuchert, M. Krychowiak, S. Kwak, T. Barbui, P. Kornejew, V. Winters, U. Hergenhanh, M. Kriete, A. Dinklage, C. Biedermann, G. Kocsis, G. Cseh, L. Zsuga, S. Bozhenkov, E. Pasch, A. Pavone, D. Gradic, V. Perseo, and W7-X Team, *Stellarator News* (2021).
- ³¹Y. Feng, F. Sardei, P. Grigull, K. McCormick, J. Kisslinger, and D. Reiter, *Nucl. Fusion* **46**, 807 (2006).
- ³²J. D. Hey, C. C. Chu, S. Brezinsek, P. Mertens, and B. Unterberg, *J. Phys. B: At., Mol. Opt. Phys.* **35**, 1525 (2002).
- ³³R. Appel, C. D. Dyer, and J. N. Lockwood, *Appl. Opt.* **41**, 2470 (2002).
- ³⁴C. A. Michael, J. Howard, and B. D. Blackwell, *Phys. Plasmas* **11**, 4008 (2004).
- ³⁵J. S. Allcock, S. A. Silburn, R. M. Sharples, J. R. Harrison, N. J. Conway, and J. W. M. Vernimmen, *Rev. Sci. Instrum.* **92**, 073506 (2021).
- ³⁶M. Servin, J. A. Quiroga, and J. M. Padilla, *Fringe Pattern Analysis for Optical Metrology* (Wiley, Weinheim, 2014).
- ³⁷P. Virtanen, R. Gommers, T. E. Oliphant, M. Haberland, T. Reddy, D. Cournapeau, E. Burovski, P. Peterson, W. Weckesser, J. Bright, S. J. Van Der Walt, M. Brett, J. Wilson, K. J. Millman, N. Mayorov, A. R. J. Nelson, E. Jones, R. Kern, E. Larson, C. J. Carey, Í. Polat, Y. Feng, E. W. Moore, J. VanderPlas, D. Laxalde, J. Perktold, R. Cimrman, I. Henriksen, E. A. Quintero, C. R. Harris, A. M. Archibald, A. H. Ribeiro, F. Pedregosa, P. Van Mulbregt *et al.*, "SciPy 1.0: Fundamental algorithms for scientific computing in Python," *Nat. Methods* **17**, 261 (2020).
- ³⁸J. Howard, F. Glass, and C. Michael, *Plasma Fusion Res.* **2**, S1014 (2007).
- ³⁹M. Krychowiak, R. König, F. Henke, T. Barbui, E. Flom, S. Kwak, J. Svensson, Y. Feng, Y. Gao, M. Jakubowski, M. Otte, F. Reimold, O. Schmitz, D. Zhang, T. S. Pedersen, and W7-X Team, in *47th EPS Conference on Plasma Physics* (European Physical Society, 2021), p. P1.1026.
- ⁴⁰S. Silburn, J. Harrison, T. Farley, J. Cavalier, S. V. Stroud, J. McGowan, A. Marignier, E. Nurse, C. Gutschow, M. Smithies, A. Wynn, and R. Doyle, *Calcam*, Zenodo (2023).
- ⁴¹C. Beidler, G. Grieger, F. Herrnegger, E. Harmeyer, J. Kisslinger, W. Lotz, H. Maassberg, P. Merkel, J. Nührenberg, F. Rau, J. Sapper, F. Sardei, R. Scardovelli, A. Schlüter, and H. Wobig, *Fusion Technol.* **17**, 148 (1990).
- ⁴²U. Neuner, K. Rahbarnia, C. Beidler, A. Dinklage, Y. Turkin, T. Stange, T. Andreeva, J. Schilling, H. Thomsen, M. Beurskens, S. Bozhenkov, K. Brunner, H. Damm, G. Fuchert, J. Geiger, U. Hergenhanh, U. Höfel, J. Knauer, M. Krychowiak, S. Kwak, A. Langenberg, N. Pablant, E. Pasch, A. Pavone, E. Scott, J. Svensson, H. Mora, and Wendelstein 7-X Team, "Measurements of the parameter dependencies of the bootstrap current in the W7-X stellarator," *Nucl. Fusion* **61**, 036024 (2021).
- ⁴³T. S. Pedersen, M. Otte, S. Lazerson, P. Helander, S. Bozhenkov, C. Biedermann, T. Klinger, R. C. Wolf, H.-S. Bosch, I. Abramovic, S. Äkäslompolo, P. Aleynikov, K. Aleynikova, A. Ali, A. Alonso, G. Anda, T. Andreeva, E. Ascasibar, J. Balduhn, M. Banduch, T. Barbui, C. Beidler, A. Benndorf, M. Beurskens, W. Biel, D. Birus, B. Blackwell, E. Blanco, M. Blatzheim, T. Bluhm, D. Böckenhoff, P. Bolgert, M. Borchardt, L.-G. Böttger, R. Brakel, C. Brandt, T. Bräuer, H. Braune, R. Burhenn, B. Buttenschön, V. Bykov, I. Calvo, A. Cappa, A. Carls, B. B. De Carvalho, F. Castejon, M. Cianciosa, M. Cole, S. Costea, G. Cseh, A. Czarnecka, A. Da Molin, E. De La Cal, A. De La Pena, S. Degenkolbe, C. Prakash Dhard, A. Dinklage, M. Dostal, M. Drevlak, P. Drewelow, P. Drews, A. Dudek, F. Durodie, A. Dzikowicka, P. Van Eeten, F. Effenberg, M. Endler, V. Erckmann, T. Estrada, N. Fahrenkamp, J. Fellingner, Y. Feng, W. Figacz, O. Ford, T. Fornal, H. Frerichs, G. Fuchert, M. Garcia-Munoz, B. Geiger, J. Geiger, N. Gierse, A. Gogoleva, B. Goncalves, D. Gradic, M. Grahl, S. Groß, H. Grote, O. Grulke, C. Guerard, M. Haas, J. Harris, H. J. Hartfuß, D. Hartmann, D. Hathiramani, B. Hein, S. Heinrich, S. Henneberg, C. Hennig, J. Hernandez, C. Hidalgo, U. Hidalgo, M. Hirsch, U. Höfel, H. Hölbe, A. Hölting, M. Houry, V. Huber, C. Ionita, B. Israeli, S. Jablonski, M. Jakubowski, A. J. Van Vuuren, H. Jenzsch, J. Kaczmarczyk, J.-P. Kallmeyer, U. Kamionka, H. Kasahara, N. Kenmochi, W. Kernbichler, C. Killer, D. Kinna, R. Kleiber, J. Knauer, F. Köchl, G. Kocsis, Y. Kolesnichenko, A. Könies, R. König, P. Kornejew, F. Köster, A. Krämer-Flecken, R. Krampitz, N. Krawczyk, T. Kremeyer, M. Krychowiak, I. Ksiazek, M. Kubkowska, G. Kühner, T. Kurki-Suonio, P. Kurz, K. Küttler, S. Kwak, M. Landreman, A. Langenberg, F. Lapayese, H. Laqua, H.-P. Laqua, R. Laube, M. Laux, H. Lentz, M. Lewerentz, Y. Liang, S. Liu, J.-F. Lobsien, J. L. Cisquella, D. Lopez-Bruna, J. Lore, A. Lorenz, V. Lutsenko, H. Maaßberg, J. Maisano-Brown, O. Marchuk, L. Marrelli, S. Marsen, N. Maruschchenko, S. Masuzaki, K. McCarthy, P. McNeely, F. Medina, D. Milojevic, A. Mishchenko, B. Missal, J. Mittelstaedt, A. Mollen, V. Moncada, T. Mönnich, D. Moseev, M. Nagel, D. Naujoks, G. H. Neilson, O. Neubauer, U. Neuner, T.-T. Ngo, H. Niemann, C. Nührenberg, J. Nührenberg, M. Ochando, K. Ogawa, J. Ongena, H. Oosterbeek, N. Pablant, D. Pacella, L. Pacios, N. Panadero, E. Pasch, I. Pastor, A. Pavone, E. Pawelec, A. Pedrosa, V. Perseo, B. Peterson, D. Pilopp, F. Pisano, M. E. Puiatti, G. Plunk, M. Preynas, J. Proll, A. P. Sitjes, F. Purps, M. Rack, K. Rahbarnia, J. Riemann, K. Riße, P. Rong, J. Rosenberger, L. Rudischhauser, K. Rummel, T. Rummel, A. Runov, N. Rust, L. Ryc, H. Saitoh, S. Satake, J. Schacht, O. Schmitz, S. Schmuck, B. Schneider, M. Schneider, W. Schneider, R. Schrittwieser, M. Schröder, T. Schröder, R. Schröder, H. W. Schumacher, B. Schweer, R. Seki, P. Sinha, S. Sipilae, C. Slaby, H. Smith, J. Sousa, A. Spring, B. Standley, T. Stange, A. Von Stechow, L. Stephey, M. Stoneking, U. Stridde, Y. Suzuki, J. Svensson, T. Szabolics, T. Szepesi, H. Thomsen, J.-M. Travere, P. Travero, H. T. Mora, H. Tsuchiya, T. Tsujimura, Y. Turkin, S. Valet, B. Van Milligen, L. Vela, J.-L. Velasco, M. Vergote, M. Vervier, H. Viebke, R. Vilbrandt, C. P. Von Thun, F. Wagner, E. Wang, N. Wang, F. Warmer, T. Wauters, L. Wegener, T. Wegner, G. Weir, J. Wendorf, U. Wenzel, A. Werner, Y. Wie, B. Wiegel, F. Wilde, T. Windisch, M. Winkler, V. Winters, A. Wright, G. Wurden, P. Xanthopoulos, I. Yamada, R. Yasuhara, M. Yokoyama, D. Zhang, M. Zilker, A. Zimbal, A. Zocco, and S. Zoletnik, *Nat. Commun.* **7**, 13493 (2016).
- ⁴⁴C. Killer, Y. Gao, V. Perseo, L. Rudischhauser, K. Hammond, B. Buttenschön, T. Barbui, B. D. Blackwell, K.-J. Brunner, P. Drews, M. Endler, J. Geiger, O. Grulke, M. Jakubowski, S. Klose, J. Knauer, A. Knieps, R. König, Y. Li, U. Neuner, H. Niemann, M. Otte, J. Schilling, A. P. Sitjes, K. Rahbarnia, T. Stange, and W7-X Team, *Plasma Phys. Controlled Fusion* **61**, 125014 (2019).
- ⁴⁵E. Thomas, U. Konopka, D. Artis, B. Lynch, S. Leblanc, S. Adams, R. L. Merlino, and M. Rosenberg, *J. Plasma Phys.* **81**, 345810206 (2015).
- ⁴⁶D. M. Kriete, V. Perseo, D. Gradic, D. A. Ennis, R. König, and D. A. Maurer, Public data set: Multi-delay coherence imaging spectroscopy optimized for ion temperature measurements in the divertor plasma of the Wendelstein 7-X stellarator (2024).